








Improved Astrophysical and Computational Oscillator Strengths for Ultraviolet P II Lines

Frances H. Cashman^{1,2} , Romas Kisielius³ , Varsha P. Kulkarni⁴ , Rasa Karpuškiene³ , and Fatima Elkhatib⁴ 

¹ Department of Physics, Presbyterian College, Clinton, SC 29325, USA; fcashman@presby.edu

² Space Telescope Science Institute, 3700 San Martin Drive, Baltimore, MD 21218, USA

³ Institute of Theoretical Physics and Astronomy, Vilnius University, Saulėtekio al.3, LT-10257 Vilnius, Lithuania

⁴ Department of Physics and Astronomy, University of South Carolina, Columbia, SC 29208, USA

Received 2023 July 21; revised 2024 July 14; accepted 2024 August 2; published 2024 October 3

Abstract

Abundance measurements for the volatile element phosphorus are important for measuring the metallicity in interstellar and circumgalactic gas, where their accuracies are limited by uncertainties in the oscillator strengths. We report updated oscillator strength values for two resonant transitions of the dominant ion P II, the transitions at 961.041 and 963.801 Å, which have historically shown large uncertainties. Using a combination of observational measurements and highly accurate quasi-relativistic Hartree–Fock theoretical calculations, we present an updated oscillator strength of $f = 0.147 \pm 0.021$ for the poorly constrained P II resonant transition at 961.401 Å, which arises from the ground electronic state $3s^23p^2\ ^3P_0$ to the excited level $3s^23p3d\ ^3D_1^o$. This result utilizes archival optical spectra obtained with the Very Large Telescope for the quasar PKS 0528–250, which has a damped Ly α absorber at $z = 2.811$. We calculate a theoretical f -value = 0.153 for 961.401 Å consistent with our empirically derived value, and calculate a theoretical f -value = 1.79 for 963.801 Å. We also present theoretical oscillator strengths for the P II resonant transitions at 972.779, 1124.945, 1152.818, 1301.874, and 1532.533 Å, as well as for multiple P II fine-structure and excited-level transitions. The updated f -value for the P II 961 Å transition will be useful in future studies of P abundances, especially in sight lines where the 1152 Å line is saturated.

Unified Astronomy Thesaurus concepts: Laboratory astrophysics (2004); Ultraviolet astronomy (1736); Optical astronomy (1776); Metal line absorbers (1032); Atomic data (2216)

1. Introduction

Most chemical elements beyond helium are produced in stellar nucleosynthesis and supernova explosions. Understanding the evolution of these elements is thus fundamental to astrophysics for a number of reasons. The history of element production is directly linked to the history of star formation in galaxies. Indeed, different elements are synthesized in stars of different masses. For example, α elements such as oxygen, magnesium, silicon, and sulfur originate primarily in massive stars, while iron-group elements form mainly in Type Ia supernova explosions. Measurements of the abundances of these different elements as a function of cosmic time thus provide powerful insights for understanding how the global star formation rate and supernova explosion rate evolved with time (e.g., P. Madau & M. Dickinson 2014; E. Vangioni et al. 2015). This history of chemical enrichment in galaxies also has implications for the evolution of the intergalactic background radiation, cosmic reionization, and even the rate of binary black hole mergers (e.g., K. Nakazato et al. 2016; S. Stevenson et al. 2017; G. D. Becker et al. 2019). Furthermore, the chemical evolution of galaxies has implications for even the formation of planetary systems.

Abundance measurements for a vast range of elements have been performed in numerous astronomical objects, including the Sun, other stars, and in the interstellar medium (ISM) in the Milky Way. Measurements are also available for the ISM and the circumgalactic medium (CGM) of nearby galaxies such as

the Small Magellanic Cloud (SMC) and the Large Magellanic Cloud (LMC). Abundance measurements of the ISM and CGM are much more challenging for the more distant galaxies, but have still been accomplished using absorption-line spectroscopy of background sources such as quasars and gamma-ray bursts (GRBs). The strongest of these absorbers are the damped Ly α absorbers (DLAs) and sub-DLAs, with H I column densities of $N_{\text{HI}} \geq 2 \times 10^{20} \text{ cm}^{-2}$ and $10^{19} \leq N_{\text{HI}} < 2 \times 10^{20} \text{ cm}^{-2}$, respectively. Studies performed using the Hubble Space Telescope (HST) in the ultraviolet (UV) and ground-based telescopes in the optical have made it possible to determine element abundances in DLA/sub-DLAs, which in fact are the most precisely measured abundances in distant galaxies (e.g., J. X. Prochaska et al. 2003; V. P. Kulkarni et al. 2005, 2007, 2015; M. Rafelski et al. 2012; D. Som et al. 2015; S. Quiret et al. 2016; S. Poudel et al. 2020).

One important respect in which element abundances in the ISM and CGM of the Milky Way as well as other galaxies differ from element abundances in the Sun is that the latter are observed to be higher for some elements due to their condensation on dust grains. Depletion is much more severe for refractory elements (those with higher condensation temperatures, such as Si, Mg, Ca, Fe, Cr) than for volatile elements (such as O, P, S, Zn) in the ISM of the Milky Way, LMC, and SMC (e.g., B. D. Savage & K. R. Sembach 1996; Jenkins 2009; E. B. Jenkins & G. Wallerstein 2017). Depletion is also observed to be present in DLA/sub-DLAs even back to $z \sim 4$ (e.g., A. De Cia et al. 2016; S. Morrison et al. 2016). Accurate “dust-free” determinations of metallicity from gas-phase abundances accessible through UV and optical spectroscopy thus requires the use of weakly depleted elements, since for

these elements the gas-phase abundance is essentially the total abundance.

Even with the use of volatile elements, one major limitation affecting the accuracy of metallicity determinations is that the atomic data for many transitions of key ions are not sufficiently well determined. Specifically, the oscillator strengths of the key transitions for a number of elements have large uncertainties, or do not even have estimated uncertainties. This is a serious problem, since the column density of any atom or ion determined from absorption-line spectroscopy is inversely proportional to the oscillator strength. Indeed, uncertainties in oscillator strengths are far worse than the measurement uncertainties achieved with state-of-the-art high-resolution spectrographs on large telescopes (see, e.g., F. H. Cashman et al. 2017 and D. C. Morton 2003, for a discussion of the uncertainties).

A number of studies have been conducted in recent years to improve this situation with more accurate experimental measurements and theoretical calculations (see, e.g., S. R. Federman et al. 2007; M. A. Bautista et al. 2009; S. S. Tayal & O. Zatsarinny 2010; J. E. Lawler et al. 2013; M. P. Wood et al. 2014; R. Kisielius et al. 2014, 2015; Boissé & Bergeron 2019; A. M. Ritchey et al. 2023). Some of these studies have been for volatile elements such as P, S, and Zn. However, each of these elements has some limitations in the context of distant galaxies traced by DLA/sub-DLAs in the spectra of quasars and GRBs. For sulfur, the dominant ion of S (S II) has only three weak lines (all within the Ly α forest, which makes them susceptible to blending with HI Lyman series lines of other galaxies). For Zn, only 2 lines are available. Both of the Zn lines usually lie outside the Ly α forest, but these lines are often difficult to detect in high-redshift galaxies because of the very low cosmic abundance of Zn (>300 times smaller than the abundance of S). There are also some uncertainties in the nucleosynthetic origin of Zn (e.g., R. D. Hoffman et al. 1996; H. Umeda & K. Nomoto 2002; T. Tsujimoto & N. Nishimura 2018). These difficulties with S and Zn underscore the importance of obtaining measurements for other weakly depleted elements as well. Unfortunately, the far more abundant and weakly depleted element O also has its own problems—the most commonly observed O I line at 1302 Å (the dominant ion in cool ISM/CGM) usually lies outside the Ly α forest, and is extremely strong, and hence almost always saturated in DLA/sub-DLAs.

1.1. Why P II?

The element P offers some promise in this context. Like S, O, and Zn, P is also only weakly depleted in the Milky Way's ISM (e.g., E. B. Jenkins 2009; A. M. Ritchey et al. 2023). Furthermore, P II (the dominant ion in cool ISM/CGM) has a number of absorption lines, including two that can lie outside the Ly α forest, i.e., P II $\lambda\lambda$ 1301, 1532. Although P II λ 1301 is often blended with O I λ 1302, the transition at λ 1532 is neatly separated from transitions of other elements. Moreover, P is far less abundant than oxygen, but far more abundant than Zn (e.g., M. Asplund et al. 2009). Thus, many of the P II lines are detectable, yet not always saturated.

Yet another motivation to study P comes from the fact that it is one of the key elements for astrobiological studies. As one of the six key elements (H, C, N, O, P, S) for biological chemistry, P is essential for all living organisms. As part of the orthophosphate radical, P plays an important role in metabolism through adenosine triphosphate (ATP) and as part of the

sugar-phosphate backbone for nucleic acids including deoxyribonucleic acid (DNA) and ribonucleic acid (RNA). It is thus of great astrobiological interest that P-containing molecules such as PN, PO, HCP have also been detected in comets, circumstellar envelopes, the ISM, star-forming regions, and even extragalactic environments (e.g., M. Agúndez et al. 2007; F. Fontani et al. 2019; V. M. Rivilla et al. 2020; D. Haasler et al. 2022).

Measurements of P abundances in the parent stars of exoplanets are important for studies of habitable exoplanets and searches for life signatures on them (see N. R. Hinkel et al. 2020). For example, terrestrial planets orbiting stars with relatively low P abundances may not have adequate amount of P on the surface to support life. While P abundances in stars are difficult to measure due to the weakness of the relevant absorption lines and the lack of suitable lines in the optical region, efforts are underway to increase the number of P measurements, e.g., with the Sloan Digital Sky Survey's Apache Point Observatory Galactic Evolution Experiment (APOGEE) spectrograph in the near-IR. These efforts have revealed a population of P-rich stars whose abundance patterns are difficult to explain with current stellar nucleosynthesis models; this may have potentially interesting implications for galactic chemical evolution. Indeed, it is possible that the predecessors of such P-rich stars may have contributed substantially to the abundance of P observed on the Earth (see T. Masseron et al. 2020).

Measurements of P abundances are somewhat easier in the diffuse ISM, since the dominant ionization stage P II has transitions that are accessible in the UV. Unfortunately, it is difficult to take advantage of the full suite of measurements because the oscillator strengths for the far-ultraviolet (FUV) P II transitions, i.e., the P II $\lambda\lambda$ 961 and 963 doublet, are highly uncertain (see F. H. Cashman et al. 2017 for a brief summary of these uncertainties). If these oscillator strengths can be improved, the entire range of P II UV transitions may become useful metallicity indicators in studies of the ISM and CGM. For example, the P II 961 Å transition will be especially useful when the P II 1152 Å is saturated. The strong P II 963 Å transition will be useful in cases where the P abundance is very low. Furthermore, in this era of advancing high-redshift astronomy, these FUV transitions are pushed longward into the optical where they can be observed at high resolution. Motivated by this need for improving the atomic data for the P II FUV transitions (and thereby the P abundance measurements in the ISM/CGM), here we make a multipronged attempt toward making these improvements.

We perform our own theoretical calculations as described in Section 2. In Section 3, we present an analysis of the archival optical spectrum of quasar PKS 0528–250 (with a DLA at $z = 2.811$) obtained with the Very Large Telescope (VLT), and discuss implications for the oscillator strengths of the P II $\lambda\lambda$ 961, 963 absorption lines. Section 4 presents our results. Section 5 compares these results with other literature. Finally, Section 6 summarizes our conclusions.

2. Atomic Data Sources

Atomic spectroscopic data for P II are usually adopted from the compilation of D. C. Morton (2003) and the NIST Atomic Spectra Database (ASD; Kramida et al. 2023). The NIST database lists state-of-the-art data such as energy levels, transition wavelengths, oscillator strengths, and evaluated

resonant transition at $\lambda 1301$ is often present, yet it is often unusable because it is either mostly or completely blended with the strong O I 1302 Å transition.

2.1. New Atomic Data Calculations

To produce the atomic data needed for our investigation, we employ a quasi-relativistic Hartree–Fock approach (QRHF; P. Bogdanovich & O. Rancova 2007, 2006), which utilizes transformed radial orbitals (TROs; R. Karpuškienė et al. 2010) to achieve the necessary accuracy of level energies and transition oscillator strengths. As described in P. Bogdanovich et al. (2011), R. Kisielius et al. (2014), and P. Bogdanovich & R. Kisielius (2012), the QRHF approach enables production of atomic data suitable for line identification and absorption spectra modeling. This method employs quasi-relativistic radial orbitals (ROs) to describe one-electron wave functions for the configurations under consideration. These ROs are determined by solving QRHF equations for a conventional self-consistent field of relativistic potential with one-electron relativistic corrections for s and p electrons; see P. Bogdanovich & O. Rancova (2007, 2006). To include comparatively huge numbers of correlation corrections, the virtually excited electrons are characterized by TROs (R. Karpuškienė et al. 2010).

To explain the adopted approach, we briefly present the calculation procedure. At the start of the investigation, the QRHF equations (P. Bogdanovich & O. Rancova 2007, 2006) are solved and the ROs are determined for the excited configuration $3s^23p3d$. In this way, the ROs for the electrons up to $3d$ are determined. Further, the ROs of electrons with $4 \leq n \leq 7$, $\ell \leq 4$ are derived by solving the QRHF equations in the core $3s^23p$ potential.

The correlation corrections are included by implementing the configuration interaction (CI) method. The CI wave-function expansion is based on the sets of investigated (adjusted) and admixed configurations that are produced by promoting one or two electrons from the 3ℓ shells of the adjusted configurations to all states available from the generated RO basis. The complete basis of ROs used in our consistent and reliable calculations is constructed from the solutions of QRHF equations and from transformed ROs. The method to determine the quasi-relativistic TROs with two variational parameters is presented in R. Karpuškienė et al. (2010). In the present work, TROs are used to describe the electrons with $8 \leq n \leq 13$ and $\ell \leq 4$.

Such a wide basis of ROs allows us to construct a huge number of the admixed configurations, and consequently to include different types of correlation effects, including the core-polarization correction. The same quasi-relativistic ROs and TROs are utilized to describe electrons in all configurations of both even and odd parity. Such an identical RO basis enables us to avoid the nonorthogonality problems of ROs when the radiative transition parameters among the levels of different parity are calculated. For the calculation of the level energies, the one-electron and the two-electron relativistic corrections are included in the Breit–Pauli approximation, as it is standard in our calculations.

For the adjustment of the four even-parity $3s^23p^2$, $3s^23p4p$, $3s^23p4f$, and $3s^23p5p$ configurations, we can produce 1218, 1598, 1653, and 1598 admixed configurations, respectively, on the entire base of ROs and TROs. For the six odd-parity configurations $3s3p^3$, $3s^23p3d$, $3s^23p4s$, $3s^23p4d$, $3s^23p5s$, and

$3s^23p5d$ we include 976, 1703, 1338, 1703, 1338, and 1703 admixed configurations.

Fortunately, not all generated admixed configurations are equally important in our calculations. The configurations that have the largest influence for the calculated level energies can be selected by implementing methods described in P. Bogdanovich & R. Karpuškienė (2001). If the average weight of any particular admixed configuration is larger than a chosen selection criterion, w , that configuration is included in the CI wave-function expansion. After several attempts, we decided that a selection criterion $w = 1 \times 10^{-7}$ is the most appropriate calculation of reliable spectroscopic parameters for P II. Only 542, 658, 481, and 585 even-parity admixed configurations and 462, 725, 597, 595, 514, and 549 odd-parity ones remain after this selection procedure. Since the configurations of even parity are inseparable in our consideration, four lists of admixed configurations are combined excluding the same ones. The same combining procedure is done for six lists of the odd-parity admixed configurations. Finally, 1492 even-parity admixed configurations and 2094 odd ones are included into our CI expansion.

Each admixed configuration has two or more open shells. Therefore, the resulting number of generated CSFs is very large. The numbers of CSFs after selection of significant admixed configurations are 129,024 for the even-parity configurations and 160,770 for those of odd parity. Fortunately, for some of those CSFs, the matrix elements of the electrostatic interaction with the CSFs of the investigated configurations are equal to zero. Consequently, such CSFs can be eliminated from the level energy calculations without any loss of accuracy in the calculated results. The reduced numbers of CSFs are 27,910 for the even-parity configurations and 35,306 for those of odd parity. This method is described in full in P. Bogdanovich et al. (2002) and it is effectively used in our previous calculations.

During the calculations, we took extreme care in determining correct energy level positions and always checked for a stable and consistent calculated energy difference between close-lying and interacting fine-structure levels. As was noted previously by A. Hibbert (1988), the calculated oscillator strength values are very sensitive to this energy difference. In Table A1, we show the complete data set for the P II resonant, excited, and fine-structure transitions originating from the lowest three levels 3P_0 , 3P_1 , and 3P_2 of the ground configuration $3s^23p^2$.

3. Astrophysical Measurements

The rest-frame wavelengths of the P II transitions reside in the FUV portion of the electromagnetic spectrum. The absorption lines remain observable in the UV for nearby targets, with the lowest 961 Å transition shifted to the optical for redshifts greater than ~ 2.3 .

Of the suite of P II transitions (see Table 1), the 961 and 963 Å transitions have undergone large changes in oscillator strength over multiple theoretical studies. To the best of our knowledge, no experimental f -values exist for either transition. Table 2 summarizes the course of the changes to their values throughout the literature. Searching for an empirical constraint on the oscillator strength of these lines is the focus for the archival portion of this study. Conversely, multiple studies of the P II $\lambda 1152$ line have produced mutually consistent results (see Table 2). Thus, comparative analysis of the observed absorption profiles of these P II lines in high-resolution spectra can deliver the much needed constraints on the oscillator strengths of the uncertain 961 and 963 Å transitions by

Table 2Literature Theoretical f -values, Experimental Oscillator Strength f Measurements, and our QRHF Calculation Data for P II $\lambda\lambda 961, 963, 1152, 1301, 1532$

$f(961)$	$f(963)$	$f(1152)$	$f(1301)$	$f(1532)$	Reference
0.349	1.45	0.244	0.0127	0.00303	^a
0.595	1.80	0.251	0.0207	0.00793	^b
0.0128	1.86	0.253	0.0210	0.00693	^c
0.0219	1.84	0.250	0.0213	0.00695	^d
...	...	0.272 ± 0.029	0.0196 ± 0.002	0.00737	^e
0.153	1.79	0.254	0.0213	0.00628	^f ,TW
0.147 ± 0.021	^g ,TW

Notes. We include uncertainties for published literature values where available.

^a Theoretical data from A. Hibbert (1988; values adopted by D. C. Morton 2003).

^b Theoretical data from S. S. Tayal (2003).

^c Theoretical data from C. Froese Fischer et al. (2006).

^d Theoretical data from P. Rynkun et al. (2019).

^e Experimentally determined lab values for $\lambda\lambda 1152, 1301$ from S. R. Federman et al. (2007) and M. S. Brown et al. (2018), respectively, and an empirical value for $\lambda 1532$ based on astrophysical spectra from A. M. Ritchey et al. (2023).

^f Theoretical data for $\lambda\lambda 963, 1152, 1301, 1532$ produced from the quasi-relativistic Hartree–Fock (QRHF) approach, uncorrected for the differences between theoretical and observed transition wavelengths to facilitate comparison with other theoretical literature values; see Section 2.

^g Empirically derived f -value from the 961/1152 f -ratio observed in the $z = 2.811$ DLA associated with PKS 0528–250 and the experimental f -value for $\lambda 1152$ from S. R. Federman et al. (2007) and this work (TW).

referring to the well-determined oscillator strength of P II $\lambda 1152$.

3.1. Optical Quasar Spectroscopic Data

High-resolution spectra of quasars can be effectively used to obtain constraints on the oscillator strengths of the P II transitions. In order to identify suitable quasar sight lines, we first carried out a systematic literature search of all the papers from S. Quiret et al. (2016) to determine which of these papers discussed P II and which transitions they measured. Archival data of the quasars observed with the Ultraviolet and Visual Echelle Spectrograph (UVES) on the VLT were downloaded from the European Southern Observatory (ESO) Archive Science Portal. The corresponding data were visually inspected using the Python package `linetools` (J. X. Prochaska et al. 2017) to identify the P II lines in the quasar spectra and to initially compare their line profiles. In all spectra, P II $\lambda 963$ showed heavy blending with NI $\lambda 963$. Only two quasars featured unblended P II lines at $\lambda\lambda 961, 1152, \text{ and } 1532$; however, only one had high enough signal-to-noise to meet our criteria. We selected PKS 0528–250, a quasar with emission redshift $z_{\text{em}} = 2.779$ and a strong associated DLA at redshift $z_{\text{abs}} = 2.811$ (see Table 3 and, e.g., D. L. Jauncey et al. 1978; H. E. Smith et al. 1979, for early studies of this DLA). We obtained the coadded, continuum-normalized VLT UVES spectra covering 3042–10430 Å as constructed in the SQUAD survey (M. T. Murphy et al. 2019), downloaded from the ESO Archive Science Portal. The coadded spectrum was made from three different exposures (two exposures of 5655 s and one exposure of 1320 s), and has a spectral resolution of 6.0 km s^{-1} . The normalized spectrum was used to identify the velocity structure of the absorbing gas associated with the DLA.

3.2. Apparent Optical Depth Analysis

The absorption-line system at $z = 2.811$ toward PKS 0528–250 shows the P II $\lambda\lambda 961, 1152, \text{ and } 1532$ lines spanning $\sim 200 \text{ km s}^{-1}$ in the high-resolution UVES spectrum (see Figure 2). We employ the apparent optical depth (AOD; B. D. Savage & K. R. Sembach 1991) method to derive the

Table 3
Parameters for QSO PKS 0528–250

Quasar	z_{em}	z_{abs}	Reference
PKS 0528–250	2.779	2.811	J78; S79

Note. References for the DLA toward PKS 0528–250: (J78) D. L. Jauncey et al. (1978), (S79) H. E. Smith et al. (1979).

velocity profile of the optical depth $\tau(\nu)$, using

$$\tau(\nu) = -\ln(I_n(\nu)), \quad (1)$$

where $I_n(\nu)$ is the normalized absorption profile. Since for unsaturated lines the optical depth is proportional to the oscillator strength f , i.e., $\tau(\nu) \propto \lambda f N(\nu)$, we can define the ratio of the $\lambda\lambda 961, 1152$ f -values as

$$\frac{f_{961}}{f_{1152}} = \frac{\lambda_{1152} \tau_{961}(\nu)}{\lambda_{961} \tau_{1152}(\nu)}. \quad (2)$$

Thus, at velocities where the absorption-line profile is fully resolved, the f_{961}/f_{1152} ratio will display a visibly distinct value compared to regions affected by unresolved components or blends or noise, which will not show a definite value. The f_{961}/f_{1152} ratio is then calculated for the distinct velocity region by finding the mean of the $\lambda\tau(\nu)$ values across the respective pixels. The uncertainty of the f_{961}/f_{1152} ratio is determined by calculating the rms scatter from the mean value. We adopt the same methodology successfully utilized by Boissé & Bergeron (2019) to produce improved values for Ni II UV absorption lines using archival high-resolution ground-based spectra toward high-redshift quasars.

Before making a comparative analysis of the P II 961 and 1152 Å transitions, we first sought to check for saturation in the stronger $\lambda 1152$ line by comparing it to the weaker transition at $\lambda 1532$. Although the signal-to-noise is much lower for this weaker transition, an overplot of their AOD column density velocity profiles shows a consistent profile (see Figure 3), where we adopt the f -value for $\lambda 1152$ from S. R. Federman et al. (2007, from experimental beam-foil measurements) and the empirically derived f -value for $\lambda 1532$ from A. M. Ritchey et al. (2023).

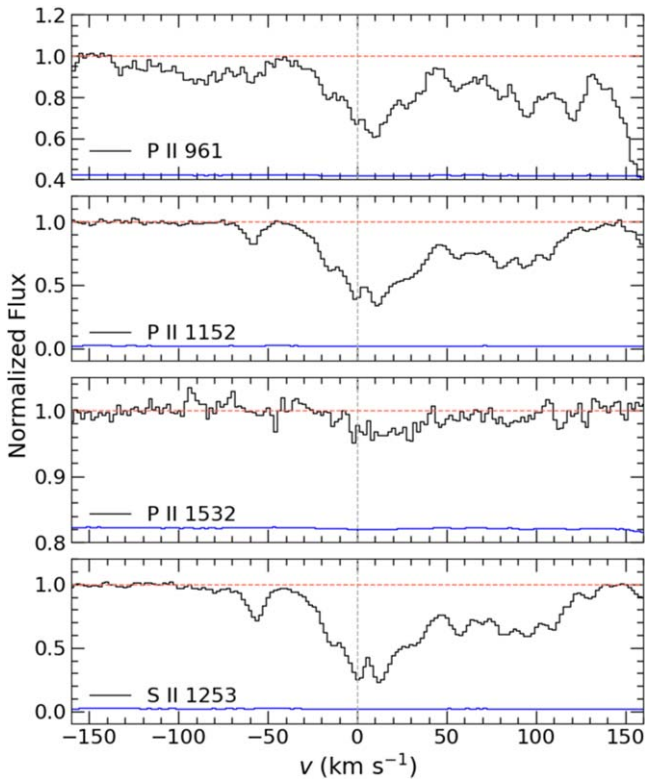


Figure 2. Velocity plots of the P II lines detected in the DLA at $z = 2.811$ associated with PKS 0528–250 in the VLT/UVES spectrum. The absorption from -70 to $+140$ km s^{-1} is associated with the DLA. The S II 1253 Å transition is included for comparison to another detected metal line. In all panels, the normalized flux is shown in black and the red horizontal line marks the level of the continuum. The blue curve is the 1σ error in the normalized flux. An offset of 0.4 and 0.8 is applied to the y-axis of the weaker 961 and 1532 Å transitions, respectively, to facilitate visualization.

Given that $\lambda 1152$ does not show noticeable saturation relative to $\lambda 1532$, we proceed with our analysis of the 961 Å transition relative to 1152 Å in order to provide an empirically derived constraint on the f -value for $\lambda 961$.

The metal-line absorption in the DLA has been studied in considerable detail over the years (see, e.g., D. C. Morton et al. 1980; L. Lu et al. 1996; J. Ge et al. 1997; S. L. Ellison et al. 2010; A. De Cia et al. 2016; S. A. Balashev et al. 2020), which aided in our analysis. This system consists of many individual velocity components with two main clumps at $z = 2.8114$ and 2.8138 . Comparison of the velocity profiles of the P II 961 Å line and the P II 1152 Å line (see top panel of Figure 4) reveals absorption in $\lambda 961$ at $v \lesssim -65$ and $v \gtrsim +90$ km s^{-1} that is not present in $\lambda 1152$. We performed a closer inspection to see if this absorption could be affecting our measurement.

Molecular hydrogen is associated with this DLA and has a velocity profile composed of two components at $z = 2.810995$ (2) and 2.811124 (2); see R. Srianand & P. Petitjean (1998) for more details. The nearest molecular hydrogen transitions are the 13–0 $P(3)$ and 15–0 $R(7)$ lines at $\lambda_{\text{rest}} = 960.449$ and 960.697 Å, respectively. The 15–0 $R(7)$ line may be responsible for the weak absorption feature near -100 km s^{-1} , however the leftmost component of the $\lambda 961$ line is redward of both the 13–0 $P(3)$ and 15–0 $R(7)$ transitions by nearly 2 and 1 Å, respectively. Therefore, we do not believe that molecular hydrogen is blended with $\lambda 961$. Other absorbers along the line

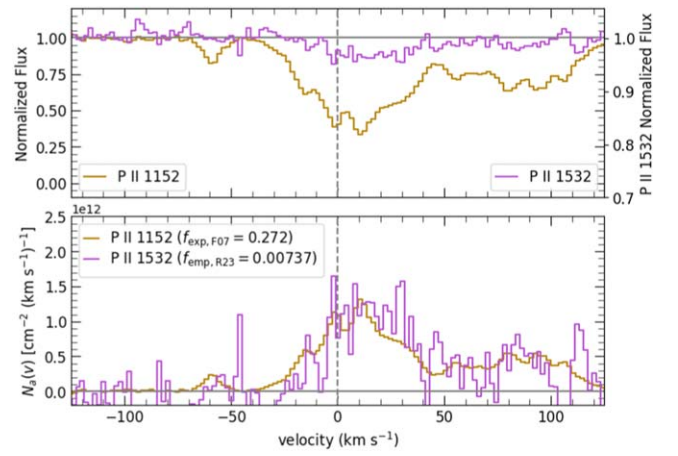


Figure 3. A comparison of the P II 1152 and 1532 Å transitions detected in the DLA at $z = 2.811$ seen toward PKS 0528–250 in the VLT/UVES spectrum. Top panel: overplot of the normalized flux of the P II 1152 (gold) and 1532 Å (pink) transitions. A secondary y-axis for the weaker $\lambda 1532$ transition is shown on the right side of the plot. Bottom panel: an overplot of the AOD column density velocity profiles, $N_d(v)$, for the P II 1152 (gold) and 1532 Å (pink) transitions using the experimental f -value from S. R. Federman et al. (2007) and the empirically derived f -value for $\lambda 1532$ from A. M. Ritchey et al. (2023).

of sight include an absorption-line system at $z = 2.53758$ and $z = 2.14077$. However, there is no intervening absorption from either of these redshifts at the wavelengths corresponding to the P II 961 Å components in question.

As this region lies shortward of the background quasar’s Ly α emission, we cannot rule out that the extra absorption at $v \lesssim -65$ and $v \gtrsim +90$ km s^{-1} seen in $\lambda 961$ is due to intervening Ly α absorption. However, we observe no visibly distinct change in the f -value ratio in our velocity region of interest from $-40 \lesssim v \lesssim +90$ km s^{-1} (see bottom panel of Figure 4), which would indicate the presence of an unresolved blend if significant Ly α absorption is indeed present.

4. Results

This section is organized into two parts. First, we show our theoretical results for the suite of P II resonant, excited-level, and fine-structure transitions originating from the 3P ground term. In the second part, we present the AOD analysis for the DLA toward quasar sight line PKS 0528–250 and the empirically derived oscillator strength for $\lambda 961$.

4.1. Theoretical Results

A new set of atomic oscillator strengths f , transition probabilities (rates) A , and transition wavelengths λ was produced by employing the QRHF approach. Section 2.1 explains the calculation methods and ways to achieve consistent results and desired accuracy of level energies and transition oscillator strengths f . The atomic data needed for the analysis and modeling of absorption spectra are listed in Table A1. Here we present the calculated wavelengths λ and absorption oscillator strengths f both for the resonant transitions and the transitions involving the fine-structure levels of the lowest term $3s^23p^2\ ^3P$. Alongside this, the emission transition rates (A -rates) and corresponding transition line strengths S are listed. For this table, we have chosen to present line data without corrections for the differences between theoretical and observed transition wavelengths. A simple formula to introduce these corrections is shown for the

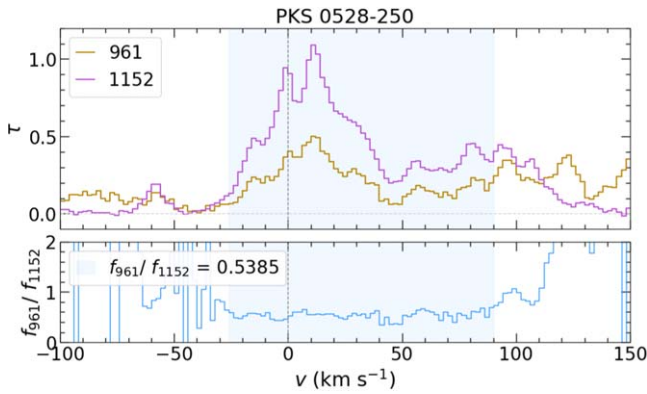


Figure 4. Absorption lines of P II $\lambda\lambda$ 961, 1152 observed in the DLA at $z_{\text{abs}} = 2.811$ toward PKS 0528–250. The top panel shows the optical depth profiles for the 961 (in gold) and 1152 Å (pink) transitions. In the bottom panel, the flat region of the curve shaded in light blue was used to calculate the f -ratio of 961/1152.

oscillator strength f -values in Section 2, and for transition rates A in M. L. Lykins et al. (2015). In any case, these corrections are small (e.g., $<0.2\%$ and $<0.8\%$ for P II $\lambda\lambda$ 961 and 1152, respectively). For the P II doublet at $\lambda\lambda$ 961, 963, we calculate $f = 0.153$ for the P II 961 Å transition and $f = 1.79$ for the 963 Å transition.

4.2. Empirical f -value for 961 Å

The UVES optical data for the $z_{\text{abs}} = 2.811$ absorber toward PKS 0528–250 cover the 961, 1152, and 1532 Å resonant transitions. For $\lambda\lambda$ 961, 1152, we calculated the AOD profile for each transition using Equation (1) and then determined the f_{961}/f_{1152} ratio at each pixel along the velocity profile in the region from -25 to $+90$ km s $^{-1}$ using Equation (2). In Figure 4, we illustrate the $\tau(v)$ profiles and the resulting f_{961}/f_{1152} ratio for the $z_{\text{abs}} = 2.811$ system toward PKS 0528–250. We find a mean value for $f_{961}/f_{1152} = 0.539 \pm 0.078$ across these pixels, where the uncertainty represents the rms scatter about the mean. Table 4 lists this observed ratio as well as our theoretically calculated f -ratio of 0.601, which is consistent with the observed f -ratio within the uncertainty margin, differing by approximately 10%.

To derive an empirical constraint on the f -value of λ 961, we calculate f_{961} by multiplying the observed f_{961}/f_{1152} ratio by the well-known f -value for λ 1152. We consider our theoretical result $f_{1152} = 0.256$ (corrected for uncertainties in the calculated wavelengths) and $f_{1152} = 0.272$ from the experimental beam-foil measurements of S. R. Federman et al. (2007). Using our theoretically calculated f -value, we derive an empirical f -value for λ 961 of $f_{961} = 0.138 \pm 0.020$, where the uncertainty reflects the highest and lowest f -values permitted by the uncertainty on f_{961}/f_{1152} from the rms scatter about the mean. Using the experimental f -value for λ 1152 of 0.272 from S. R. Federman et al. (2007), we find an f -value of $f_{961} = 0.147 \pm 0.021$. Both empirical f -values are consistent with each other within their error margins, and are also consistent with our independent theoretical calculation of $f_{961} = 0.153$. Moreover, the empirical f -value of 0.147 only differs from our independent theoretical calculation by 3.9%. Going forward, we adopt our empirical f -value $= 0.147 \pm 0.021$ derived with the f -value for λ 1152 of 0.272 from S. R. Federman et al. (2007) since these data are experimentally determined.

Table 4

Ratio of f -values and the Derived Values of the Oscillator Strengths for the P II 961 Å Transition

Target	$f(961)/f(1152)$
PKS 0528–250 (observed)	$0.5385 \pm 0.0780^{\text{a}}$
QRHF (theory)	0.601
f -values	
$f(961)$ (empirical) ^b	0.138 ± 0.020
$f(961)$ (empirical) ^c	0.147 ± 0.021
$f(961)$ (QRHF theory)	0.153

Notes.

^a The error on the mean f_{961}/f_{1152} ratio is the rms scatter about the mean; see Section 4.2 for more details.

^b Our theoretical f -value for λ 1152 of 0.2559 (corrected for uncertainties in the calculated wavelengths) was used to derive the f_{961} value from the average observed f_{961}/f_{1152} ratio.

^c The experimental beam-foil measurement f -value for λ 1152 of 0.272 was used to derive the f_{961} value from the average observed f_{961}/f_{1152} ratio.

5. Discussion

To evaluate our new result for P II 961 Å in context with other values from the literature, we applied a Voigt profile fit of the λ 1152 transition in the high-resolution spectrum of PKS 0528–250 to the λ 961 transition using f -values from this work and the literature. We used the Voigt profile fitting software VPFIT (v.12.2; R. F. Carswell & J. K. Webb 2014) to perform all fits.

The high-resolution spectrum of PKS 0528–250 has been well studied, with recently published fits to many metal lines from S. A. Balashev et al. (2020). We adopt their singly ionized species component redshifts and b -values to produce a Voigt profile fit to the λ 1152 transition and determine the column density (see the top panel of Figure 5), using the experimentally determined f -value from S. R. Federman et al. (2007). We find $\log N(\text{P II}/\text{cm}^{-2}) = 13.93 \pm 0.04$. The complete Voigt profile for λ 1152 (i.e., component redshifts, b -values, and column densities) is then applied to the λ 961 transition using f -values from this work (TW) and the literature (A. Hibbert 1988; S. S. Tayal 2003; C. Froese Fischer et al. 2006; P. Rynkun et al. 2019). We find that the lowest f -values from C. Froese Fischer et al. (2006) and P. Rynkun et al. (2019) noticeably underfit the profile (see the bottom panel of Figure 5). Likewise, the highest f -values from A. Hibbert (1988) and S. S. Tayal (2003) produce a significantly overfitted profile to the data. However, both our empirical and independent theoretical calculation for f_{961} provide a good fit to the data.

To quantify the goodness-of-fit, we then performed a simultaneous fit to both the $\lambda\lambda$ 961, 1152 transitions using f -values for λ 961 ranging from 0.050 to 0.250 in steps of 0.005, which encompasses all of the f -values considered in this work. We used the same component redshifts and b -values from the fit to λ 1152 with the f -value from S. R. Federman et al. (2007) as before, except we excluded velocities outside the region $-40 \lesssim v \lesssim +85$, which showed signs of possible blending with Ly α , as discussed in Section 4.2. We then recorded the resulting normalized χ^2 statistic produced by VPFIT from the simultaneous Voigt profile fit, which VPFIT defines as the χ^2 statistic divided by the number of degrees of freedom. The results are shown in Figure 6. For the f -values of C. Froese Fischer et al. (2006), P. Rynkun et al. (2019),

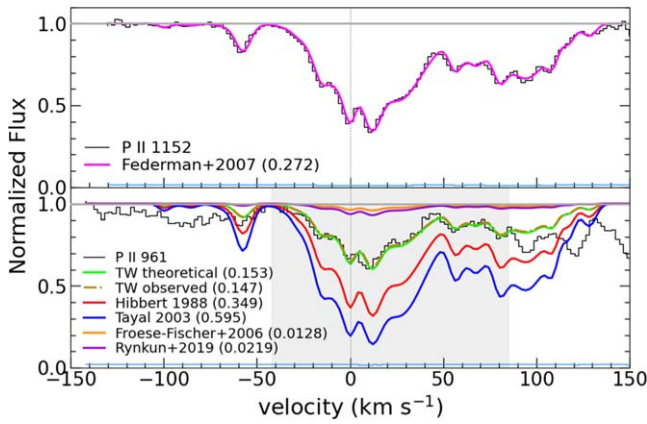


Figure 5. Top panel: Voigt profile fit to the P II 1152 transition observed in the DLA at $z_{\text{abs}} = 2.811$ toward PKS 0528–250. The normalized flux and 1σ error in the flux are shown in black and light blue, respectively. The magenta curve is the profile fit to the data resulting from adopting the published component redshifts and b -values from S. A. Balashev et al. (2020) and utilizing the experimental f -value of S. R. Federman et al. (2007) to determine the column density. Bottom panel: same as top panel, except using the range of f -values from this work (TW) and the literature in order to compare their resulting Voigt profiles. The shaded gray bar from $-40 \lesssim v \lesssim +90$ shows the region common to $\lambda\lambda 961, 1152$ (see Section 3.1). The lowest f -values from C. Froese Fischer et al. (2006) and P. Rynkun et al. (2019) produce the orange and purple profiles, respectively, and noticeably underpredict the P II column density. The highest f -values from A. Hibbert (1988) and S. S. Tayal (2003) produce the red and blue profiles, respectively, and significantly overpredict the column density. The f -values from this work produce the green (theoretical) and brown (observed) profiles, which closely match the observed data.

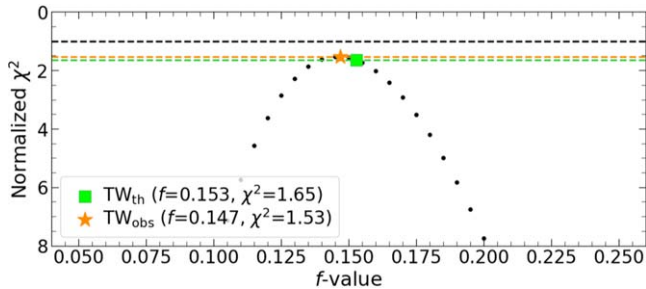


Figure 6. The normalized χ^2 results from VPFIT for the Voigt profile fit to the P II 961 Å transition seen in the $z = 2.811$ DLA toward PKS 0528–250, with f -values ranging from 0.050 to 0.250 in steps of 0.005 (black scatter points). The horizontal black dashed line is $\chi^2 = 1$. The horizontal green square and horizontal dashed line marks the χ^2 using the theoretical f -value for 961 Å from this work (0.153). The orange star and horizontal dashed line mark the χ^2 for the f -value observationally derived (0.147) from the f -ratio measured in the DLA toward PKS 0528–250. For the f -values of C. Froese Fischer et al. (2006), P. Rynkun et al. (2019), A. Hibbert (1988), and S. S. Tayal (2003), we find high normalized χ^2 values of 52.3, 126.7, 93.1, and 78.4, respectively.

A. Hibbert (1988), and S. S. Tayal (2003), we find high normalized χ^2 values of 52.3, 126.7, 93.1, and 78.4, respectively. We find the lowest normalized $\chi^2 = 1.53$ for the empirically derived $f_{961} = 0.147$. This result is not unexpected for this test as the f -value was derived from our observed f -ratio using f_{1152} from S. R. Federman et al. (2007), which defines the fit parameters for the $\lambda 1152$ transition. However, we emphasize that our independent theoretical calculation yielding $f_{961} = 0.153$ has a normalized $\chi^2 = 1.65$, differing by only 0.12 from the normalized χ^2 of the empirically derived $f_{961} = 0.147$.

Of the suite of resonant P II UV transitions, $\lambda 961$ and $\lambda 963$ have the highest variance in theoretical values historically (see Table 2). We have attempted to rectify this issue for both transitions in this work using a combination of astrophysical

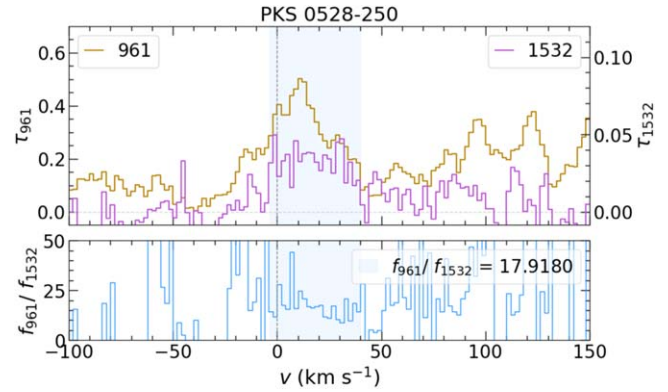


Figure 7. Absorption lines of P II $\lambda\lambda 961, 1532$ observed in the DLA at $z_{\text{abs}} = 2.811$ toward PKS 0528–250. The top panel shows the optical depth profiles for the 961 (in gold) and 1532 Å (pink) transitions. In the bottom panel, the flat region of the curve shaded in light blue was used to calculate the f -ratio of 961/1532.

observations and theoretical calculations, but were unable to make improvements for the transition at $\lambda 963$ (upper state $3s^2 3p 3d^3 P_1$) because we were unable to find a sight line that showed unblended or unsaturated interstellar absorption. In the PKS 0528–250 sight line, $\lambda 963$ is heavily saturated and in close proximity to the strong N I triplet at 963 Å. However, given that our set of theoretical QRHF calculations have shown close agreement with the observed $\lambda\lambda 961/1152$ f -ratio (theoretical $f_{961}/f_{1152} = 0.601$, observed $f_{961}/f_{1152} = 0.539$), we can recommend our theoretical f -value for $\lambda 963$ of 1.79, which is consistent with the theoretical calculations of C. Froese Fischer et al. (2006), P. Rynkun et al. (2019), and S. S. Tayal (2003); see Table 2.

Additionally, we sought to independently confirm the oscillator strength for P II $\lambda 961$ by calculating another observed line strength ratio with $\lambda 961$. Out of the other resonant P II transitions, $\lambda 1532$ offers the only other possible f -ratio in our sample due to various issues. The P II transition at 972 Å is blended with H I Lyman γ at 972 Å, which is very strong in the DLA. The P II line at 1124 Å is too weak to be detected, and P II $\lambda 1301$ is blended with the strong O I $\lambda 1302$ transition. Luckily, the optical UVES spectrum of PKS 0528–250 covers both the redshifted 961 and 1532 Å transitions in the $z_{\text{DLA}} = 2.811$ DLA (see Figure 2). However, the P II $\lambda 1532$ transition is very weak and shows low signal-to-noise.

We measure $f_{961}/f_{1532} = 17.918$ with a very large rms scatter about the mean of 7.623, noting that there are several spikes and dips in the f -ratio in the velocity region of interest as a result of the low signal-to-noise for P II $\lambda 1532$ (see Figure 7). Our theoretical QRHF calculations find $f_{961}/f_{1532} = 24.352$, which is consistent with the higher end of our observed f -ratio. As with P II $\lambda 1152$, the theoretical f -value for $\lambda 1532$ is also well known historically. We use our QRHF result of $f_{1532} = 0.00628$ to estimate the f -value for $\lambda 961$ and find $f_{961} = 0.113 \pm 0.0479$, where the uncertainty reflects the highest and lowest f -value allowed by the rms scatter. Moreover, using the observationally derived $f_{1532} = 0.00737$ from A. M. Ritchey et al. (2023), as shown in Table 2, we determine $f_{961} = 0.132 \pm 0.0562$. Thus, we find that $f_{961} = 0.147$ derived from our observed f_{961}/f_{1532} ratio in the DLA is consistent with f_{961} derived from our f_{961}/f_{1152} ratio within the margin of error.

We emphasize that our QRHF calculations for the oscillator strengths of P II $\lambda\lambda 1152, 1301, \text{ and } 1532$ agree very well with

the earlier calculations of C. Froese Fischer et al. (2006), A. M. Ritchey et al. (2023), P. Rynkun et al. (2019), and S. S. Tayal (2003), as shown in Table 2. A larger discrepancy, however, is seen with the data from the early calculations of A. Hibbert (1988). Our calculations for P II $\lambda\lambda 1152, 1301$ are also in agreement with the experimental values from S. R. Federman et al. (2007) and M. S. Brown et al. (2018), respectively.

The improvement in the oscillator strengths of the rest-frame FUV P II 961 and 963 Å transitions from our work should be helpful for future studies of interstellar P abundances in the ISM of the Milky Way, LMC, SMC, and indeed any galaxy, including the DLA/sub-DLA absorbers in sight lines to quasars and GRB afterglows. Current studies of P abundances generally rely on the $\lambda\lambda 1152, 1301, 1532$ transitions. However, P II $\lambda 1301$ can be blended with O I $\lambda 1302$, and P II $\lambda 1532$ (as the weakest) can result in nondetections in diffuse gas. In such cases, as the only other resonant transition with a weaker oscillator strength than $\lambda 1152$, the $\lambda 961$ transition will be especially useful if $\lambda 1152$ is saturated.

6. Conclusions

We derive an oscillator strength for the resonant P II 961 Å transition arising from the ground electronic state $3s^2 3p^2 \ ^3P_0$ to the excited level $3s^2 3p 3d \ ^3D_1$ of $f = 0.147 \pm 0.021$ from optical spectroscopic observations. We theoretically calculate an oscillator strength for P II 961 Å of $f = 0.153$ from QRHF theoretical calculations, which is consistent within the margin of error. We also theoretically determine an oscillator strength for the resonant P II 963 Å transition arising from the ground electronic state $3s^2 3p^2 \ ^3P_0$ to the excited level $3s^2 3p 3d \ ^3P_1$ of $f = 1.79$. Historically, theoretical calculations have given widely varying values for the f -value of $\lambda 961$ because of uncertainties arising from how close its excited $3s^2 3p 3d \ ^3D_1$ state energy is to the excited $3s^2 3p 3d \ ^3P_1$ state energy for the much stronger resonant P II $\lambda 963$ transition (see Figure 1). Utilizing high-resolution optical spectra for the DLA toward PKS 0528–250, we are able to constrain the large pool of possible theoretical results to produce a converged data set for the P II resonant, excited, and fine-structure transitions originating from the lowest three levels $^3P_0, ^3P_1,$ and 3P_2 of the ground configuration $3s^2 3p^2$ (see Table A1).

The improvement in the oscillator strengths of the FUV P II 961 and 963 Å transitions will be helpful for studies of

interstellar P abundances in galaxies. As the strength of $\lambda 961$ lies between the weakest $\lambda 1532$ transition and the often blended $\lambda 1301$ transition (with O I $\lambda 1302$ Å), this improved value for $\lambda 961$ offers an additional option for determining P abundances in environments where $\lambda 1152$ is saturated. More accurate P II column densities determined using our results would enable more accurate determination of P depletion on dust grains and of P abundances in the ISM of local as well as distant galaxies, providing more secure assessments of the evolution of metallicity with cosmic time, and thus placing additional constraints on the cosmic star formation history.

Acknowledgments

We gratefully acknowledge support from the National Science Foundation grant AST/2009811 (PI: Kulkarni). Atomic data for P II were computed on the high-performance computing cluster HYDRA-2 at the Institute of Theoretical Physics and Astronomy, Faculty of Physics, Vilnius University. We are grateful to Dr. P. Rynkun for sharing their calculation data with us. We thank Dr. Sapna Mishra for valuable conversations. We also wish to thank the reviewers for their highly constructive and helpful feedback on this paper.

The data shown in Figure 1 are available at the NIST Atomic Spectra Database (Kramida et al. 2023). The spectrum of PKS 0528–250 is available from the ESO Archive Science Portal.

Facility: VLT:Kueyen

Software: astropy (Astropy Collaboration et al. 2013, 2018), CLOUDY (G. J. Ferland et al. 2017), linetools (J. X. Prochaska et al. 2017), VPFIT (R. F. Carswell & J. K. Webb 2014)

Appendix Supplemental Data

A data table of the resonant, excited, and fine-structure transitions originating from the lowest three levels $^3P_0, ^3P_1,$ and 3P_2 of the ground configuration $3s^2 3p^2$ are shown in Table A1, where we present the theoretical line wavelengths, absorption oscillator strengths, emission transition probabilities, and transition line strengths. The data are presented without energy corrections caused by the difference between theoretical and observed level energies so that users may use their preferred observed wavelength in such a correction. Please see Section 2 for details on applying a correction to the f -values.






Table A1
 P II Theoretical Line Wavelengths λ , Absorption Oscillator Strengths f , Emission Transition Probabilities (Rates), and Transition Line Strengths S

Lower State	Upper State	λ (Å)	f	A (s ⁻¹)	S (au)
$3s^2 3p^2 \ ^3P_2$	$3s^2 3p3d \ ^1F_3$	932.43	1.25(-4)	6.90(+5)	1.93(-3)
$^a 3s^2 3p^2 \ ^3P_0$	$3s^2 3p3d \ ^3D_1$	959.75	1.53(-1)	3.69(+8)	4.83(-1)
$3s^2 3p^2 \ ^3P_1$	$3s^2 3p3d \ ^3P_2$	960.85	3.84(-1)	1.66(+9)	3.64(+0)
$3s^2 3p^2 \ ^3P_1$	$3s^2 3p3d \ ^3D_1$	961.17	4.86(-1)	3.51(+9)	4.62(+0)
$3s^2 3p^2 \ ^3P_1$	$3s^2 3p3d \ ^3P_0$	962.10	1.87(-1)	4.05(+9)	1.78(+0)
$^a 3s^2 3p^2 \ ^3P_0$	$3s^2 3p3d \ ^3P_1$	962.18	1.79(+0)	4.29(+9)	5.66(+0)
$3s^2 3p^2 \ ^3P_2$	$3s^2 3p3d \ ^3P_2$	963.50	5.38(-1)	3.86(+9)	8.53(+0)
$3s^2 3p^2 \ ^3P_1$	$3s^2 3p3d \ ^3P_1$	963.61	1.08(-2)	7.80(+7)	1.03(-1)
$3s^2 3p^2 \ ^3P_2$	$3s^2 3p3d \ ^3D_1$	963.82	1.11(-1)	1.33(+9)	1.77(+0)
$3s^2 3p^2 \ ^3P_2$	$3s^2 3p3d \ ^3D_3$	964.02	1.19(+0)	6.09(+9)	1.88(+1)
$3s^2 3p^2 \ ^3P_1$	$3s^2 3p3d \ ^3D_2$	964.71	9.08(-1)	3.90(+9)	8.65(+0)
$3s^2 3p^2 \ ^3P_2$	$3s^2 3p3d \ ^3P_1$	966.26	3.75(-2)	4.47(+8)	5.97(-1)
$3s^2 3p^2 \ ^3P_2$	$3s^2 3p3d \ ^3D_2$	967.37	9.49(-2)	6.77(+8)	1.51(+0)
$^a 3s^2 3p^2 \ ^3P_0$	$3s^2 3p3d \ ^1P_1$	970.03	4.16(-2)	9.84(+7)	1.33(-1)
$3s^2 3p^2 \ ^3P_1$	$3s^2 3p3d \ ^1P_1$	971.48	1.20(-3)	8.46(+6)	1.15(-2)
$3s^2 3p^2 \ ^3P_2$	$3s^2 3p3d \ ^1P_1$	974.18	1.58(-3)	1.85(+7)	2.53(-2)
$^a 3s^2 3p^2 \ ^3P_0$	$3s^2 3p4s \ ^1P_1$	1131.32	1.98(-3)	3.50(+6)	7.38(-3)
$3s^2 3p^2 \ ^3P_1$	$3s^2 3p4s \ ^1P_1$	1133.29	5.17(-4)	2.69(+6)	5.80(-3)
$3s^2 3p^2 \ ^3P_2$	$3s^2 3p4s \ ^1P_1$	1136.97	1.81(-4)	1.56(+6)	3.40(-3)
$3s^2 3p^2 \ ^3P_1$	$3s^2 3p3d \ ^3F_2$	1139.38	4.89(-5)	1.51(+5)	5.51(-4)
$3s^2 3p^2 \ ^3P_2$	$3s^2 3p3d \ ^3F_3$	1141.15	8.34(-5)	3.05(+5)	1.57(-3)
$3s^2 3p^2 \ ^3P_2$	$3s^2 3p3d \ ^3F_2$	1143.10	1.03(-5)	5.27(+4)	1.94(-4)
$3s^2 3p^2 \ ^3P_1$	$3s^2 3p4s \ ^3P_2$	1159.30	1.08(-1)	3.21(+8)	1.23(+0)
$^a 3s^2 3p^2 \ ^3P_0$	$3s^2 3p4s \ ^3P_1$	1161.46	2.54(-1)	4.19(+8)	9.73(-1)
$3s^2 3p^2 \ ^3P_2$	$3s^2 3p4s \ ^3P_2$	1163.15	1.93(-1)	9.52(+8)	3.70(+0)
$3s^2 3p^2 \ ^3P_1$	$3s^2 3p4s \ ^3P_1$	1163.54	6.33(-2)	3.12(+8)	7.27(-1)
$3s^2 3p^2 \ ^3P_1$	$3s^2 3p4s \ ^3P_0$	1165.28	8.53(-2)	1.26(+9)	9.81(-1)
$3s^2 3p^2 \ ^3P_2$	$3s^2 3p4s \ ^3P_1$	1167.42	6.42(-2)	5.24(+8)	1.23(+0)
$3s^2 3p^2 \ ^3P_1$	$3s^2 3p3d \ ^1D_2$	1286.60	1.59(-4)	3.84(+5)	2.02(-3)
$3s^2 3p^2 \ ^3P_2$	$3s^2 3p3d \ ^3D_2$	1291.34	1.70(-4)	6.81(+5)	3.62(-3)
$^a 3s^2 3p^2 \ ^3P_0$	$3s3p^3 \ ^3P_1$	1309.32	2.13(-2)	2.76(+7)	9.18(-2)
$3s^2 3p^2 \ ^3P_1$	$3s3p^3 \ ^3P_0$	1311.62	7.13(-3)	8.30(+7)	9.24(-2)
$3s^2 3p^2 \ ^3P_1$	$3s3p^3 \ ^3P_1$	1311.97	5.62(-3)	2.18(+7)	7.28(-2)
$3s^2 3p^2 \ ^3P_1$	$3s3p^3 \ ^3P_2$	1312.84	7.98(-3)	1.85(+7)	1.03(-1)
$3s^2 3p^2 \ ^3P_2$	$3s3p^3 \ ^3P_1$	1316.90	4.92(-3)	3.15(+7)	1.07(-1)
$3s^2 3p^2 \ ^3P_2$	$3s3p^3 \ ^3P_2$	1317.77	1.49(-2)	5.72(+7)	3.23(-1)
$^a 3s^2 3p^2 \ ^3P_0$	$3s3p^3 \ ^3D_1$	1545.75	6.28(-3)	5.84(+6)	3.20(-2)
$3s^2 3p^2 \ ^3P_1$	$3s3p^3 \ ^3D_2$	1549.22	4.73(-3)	7.89(+6)	7.24(-2)
$3s^2 3p^2 \ ^3P_1$	$3s3p^3 \ ^3D_1$	1549.44	1.37(-3)	3.80(+6)	2.10(-2)
$3s^2 3p^2 \ ^3P_2$	$3s3p^3 \ ^3D_3$	1555.70	5.02(-3)	9.87(+6)	1.28(-1)
$3s^2 3p^2 \ ^3P_2$	$3s3p^3 \ ^3P_2$	1556.11	7.21(-4)	1.99(+6)	1.85(-2)
$3s^2 3p^2 \ ^3P_2$	$3s3p^3 \ ^3D_1$	1556.33	4.22(-5)	1.94(+5)	1.08(-3)
$3s^2 3p^2 \ ^3P_1$	$3s3p^3 \ ^5S_2$	2286.34	2.02(-6)	1.55(+3)	4.57(-5)
$3s^2 3p^2 \ ^3P_2$	$3s3p^3 \ ^5S_2$	2301.36	3.51(-6)	4.42(+3)	1.33(-4)

Notes. The data are presented without energy corrections caused by the difference between theoretical and observed level energies. Resonant lines are marked with a dagger.

^a Notation a.bc(d) stands for a.bc × 10^d.

ORCID iDs

Frances H. Cashman  <https://orcid.org/0000-0003-4237-3553>
 Romas Kisielius  <https://orcid.org/0000-0001-9611-8297>
 Varsha P. Kulkarni  <https://orcid.org/0000-0002-2587-2847>
 Rasa Karpuškienė  <https://orcid.org/0000-0002-6952-0042>
 Fatima Elkhatab  <https://orcid.org/0009-0000-4780-2703>

References

- Agúndez, M., Cernicharo, J., & Guélin, M. 2007, *ApJL*, **662**, L91
 Asplund, M., Grevesse, N., Sauval, A. J., & Scott, P. 2009, *ARA&A*, **47**, 481
 Astropy Collaboration, Price-Whelan, A. M., Sipőcz, B. M., et al. 2018, *AJ*, **156**, 123
 Astropy Collaboration, Robitaille, T. P., Tollerud, E. J., et al. 2013, *A&A*, **558**, A33
 Balashev, S. A., Ledoux, C., Noterdaeme, P., et al. 2020, *MNRAS*, **497**, 1946
 Bautista, M. A., Quinet, P., Palmeri, P., et al. 2009, *A&A*, **508**, 1527
 Becker, G. D., Pettini, M., Rafelski, M., et al. 2019, *ApJ*, **883**, 163
 Bogdanovich, P., & Karpuškienė, R. 2001, *CoPhC*, **134**, 321
 Bogdanovich, P., Karpuškienė, R., & Momkauskaitė, A. 2002, *CoPhC*, **143**, 174
 Bogdanovich, P., & Kisielius, R. 2012, *ADNDT*, **98**, 557
 Bogdanovich, P., & Rancova, O. 2006, *PhRvA*, **74**, 052501
 Bogdanovich, P., & Rancova, O. 2007, *PhRvA*, **76**, 012507
 Bogdanovich, P., Rancova, O., & Štikonas, A. 2011, *PhyS*, **83**, 065302
 Boissé, P., & Bergeron, J. 2019, *A&A*, **622**, A140
 Brown, M. S., Alkhatay, R. B., Irving, R. E., et al. 2018, *ApJ*, **868**, 42
 Carswell, R. F., & Webb, J. K. 2014, VPFIT: Voigt Profile Fitting Program, Astrophysics Source Code Library, ascl:1408.015

- Cashman, F. H., Kulkarni, V. P., Kisielius, R., Ferland, G. J., & Bogdanovich, P. 2017, *ApJS*, **230**, 8
- De Cia, A., Ledoux, C., Mattsson, L., et al. 2016, *A&A*, **596**, A97
- Ellison, S. L., Prochaska, J. X., Hennawi, J., et al. 2010, *MNRAS*, **406**, 1435
- Federman, S. R., Brown, M., Torok, S., et al. 2007, *ApJ*, **660**, 919
- Ferland, G. J., Chatzikos, M., Guzmán, F., et al. 2017, *RMxAA*, **53**, 385
- Fontani, F., Rivilla, V. M., van der Tak, F. F. S., et al. 2019, *MNRAS*, **489**, 4530
- Froese Fischer, C., Tachiev, G., & Irimia, A. 2006, *ADNDT*, **92**, 607
- Ge, J., Bechtold, J., Walker, C., & Black, J. H. 1997, *ApJ*, **486**, 727
- Haasler, D., Rivilla, V. M., Martín, S., et al. 2022, *A&A*, **659**, A158
- Hibbert, A. 1988, *Phys*, **38**, 37
- Hinkel, N. R., Hartnett, H. E., & Young, P. A. 2020, *ApJL*, **900**, L38
- Hoffman, R. D., Woosley, S. E., Fuller, G. M., & Meyer, B. S. 1996, *ApJ*, **460**, 478
- Jauncey, D. L., Wright, A. E., Peterson, B. A., & Condon, J. J. 1978, *ApJL*, **221**, L109
- Jenkins, E. B. 2009, *ApJ*, **700**, 1299
- Jenkins, E. B., & Wallerstein, G. 2017, *ApJ*, **838**, 85
- Karpušienė, R., Rancova, O., & Bogdanovich, P. 2010, *JPhB*, **43**, 085002
- Kisielius, R., Kulkarni, V. P., Ferland, G. J., Bogdanovich, P., & Lykins, M. L. 2014, *ApJ*, **780**, 76
- Kisielius, R., Kulkarni, V. P., Ferland, G. J., et al. 2015, *ApJ*, **804**, 76
- Kramida, A., Ralchenko, Y., Reader, J. & NIST ASD Team 2023, NIST Atomic Spectra Database (version 5.11), v5.11, National Institute of Standards and Technology, Gaithersburg, MD, doi:10.18434/T4W30F
- Kulkarni, V. P., Fall, S. M., Lauroesch, J. T., et al. 2005, *ApJ*, **618**, 68
- Kulkarni, V. P., Khare, P., Péroux, C., et al. 2007, *ApJ*, **661**, 88
- Kulkarni, V. P., Som, D., Morrison, S., et al. 2015, *ApJ*, **815**, 24
- Lawler, J. E., Guzman, A., Wood, M. P., Sneden, C., & Cowan, J. J. 2013, *ApJS*, **205**, 11
- Lu, L., Sargent, W. L. W., Barlow, T. A., Churchill, C. W., & Vogt, S. S. 1996, *ApJS*, **107**, 475
- Lykins, M. L., Ferland, G. J., Kisielius, R., et al. 2015, *ApJ*, **807**, 118
- Madau, P., & Dickinson, M. 2014, *ARA&A*, **52**, 415
- Martin, W. C. 1959, *JOSA*, **49**, 1071
- Masseron, T., García-Hernández, D. A., Santoveña, R., et al. 2020, *NatCo*, **11**, 3759
- Morrison, S., Kulkarni, V. P., Som, D., et al. 2016, *ApJ*, **830**, 158
- Morton, D. C. 2003, *ApJS*, **149**, 205
- Morton, D. C., Jian-Sheng, C., Wright, A. E., Peterson, B. A., & Jauncey, D. L. 1980, *MNRAS*, **193**, 399
- Murphy, M. T., Kacprzak, G. G., Savorgnan, G. A. D., & Carswell, R. F. 2019, *MNRAS*, **482**, 3458
- Nakazato, K., Niino, Y., & Sago, N. 2016, *ApJ*, **832**, 146
- Poudel, S., Kulkarni, V. P., Cashman, F. H., et al. 2020, *MNRAS*, **491**, 1008
- Prochaska, J. X., Gawiser, E., Wolfe, A. M., Castro, S., & Djorgovski, S. G. 2003, *ApJL*, **595**, L9
- Prochaska, J. X., Tejos, N., Crighton, N., et al. 2017, Linetools/Linetools: Third Minor Release, v0.3, Zenodo doi:10.5281/zenodo.1036773
- Quiret, S., Péroux, C., Zafar, T., et al. 2016, *MNRAS*, **458**, 4074
- Rafelski, M., Wolfe, A. M., Prochaska, J. X., Neeleman, M., & Mendez, A. J. 2012, *ApJ*, **755**, 89
- Ritchey, A. M., Brown, J. M., Federman, S. R., & Sonnentrucker, P. 2023, *ApJ*, **948**, 139
- Rivilla, V. M., Drozdovskaya, M. N., Altwegg, K., et al. 2020, *MNRAS*, **492**, 1180
- Rynkun, P., Radžiūtė, L., Gaigalas, G., & Jönsson, P. 2019, *A&A*, **622**, A167
- Savage, B. D., & Sembach, K. R. 1991, *ApJ*, **379**, 245
- Savage, B. D., & Sembach, K. R. 1996, *ARA&A*, **34**, 279
- Smith, H. E., Jura, M., & Margon, B. 1979, *ApJ*, **228**, 369
- Som, D., Kulkarni, V. P., Meiring, J., et al. 2015, *ApJ*, **806**, 25
- Srianand, R., & Petitjean, P. 1998, *A&A*, **335**, 33
- Stevenson, S., Vigna-Gómez, A., Mandel, I., et al. 2017, *NatCo*, **8**, 14906
- Tayal, S. S. 2003, *ApJS*, **146**, 459
- Tayal, S. S., & Zatsarinny, O. 2010, *ApJS*, **188**, 32
- Tsujimoto, T., & Nishimura, N. 2018, *ApJL*, **863**, L27
- Umeda, H., & Nomoto, K. 2002, *ApJ*, **565**, 385
- Vangioni, E., Olive, K. A., Prestegard, T., et al. 2015, *MNRAS*, **447**, 2575
- Wood, M. P., Lawler, J. E., Sneden, C., & Cowan, J. J. 2014, *ApJS*, **211**, 20